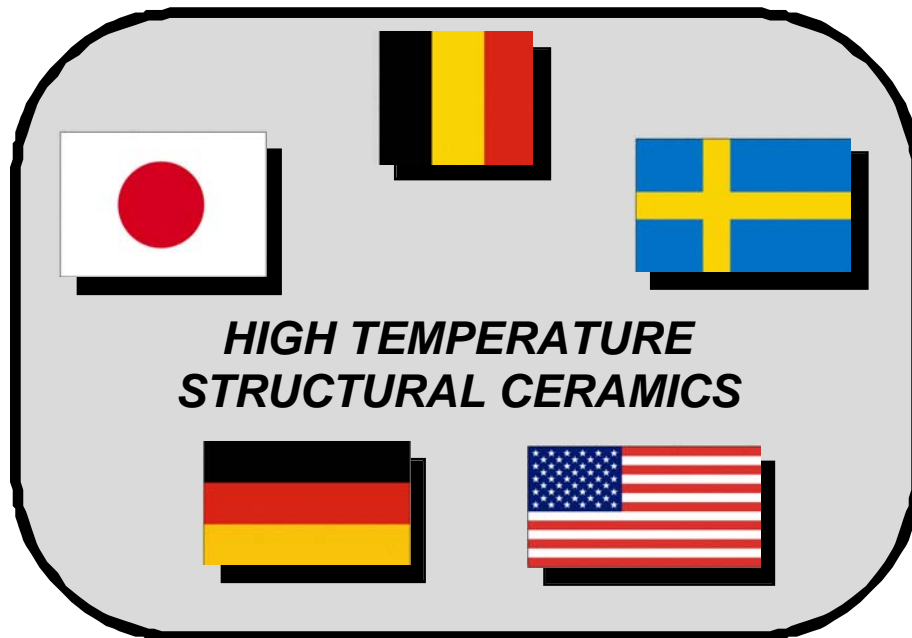


# **Thermal and Mechanical Fatigue Testing of Advanced Ceramics - Subtask 11**

International Energy Agency Implementing Agreement  
For A Programme Of Research And Development On  
Advanced Materials For Transportation Applications



**Final Report**

**March 2004**

---

---

**This document contains information whose distribution is governed by an International Energy Agency Implementing Agreement for a Co-operative Programme of Research and Development on High Temperature Materials for Automotive Engines and Other Conservation Applications (IEA Annex II), between Belgium, Germany, Japan, Sweden, and the United States. This Report shall not be disseminated to any parties other than the Participants in this Annex Agreement for a one-year period commencing from the publication date unless specifically agreed to by the Executive Committee of IEA Annex II. Following the one-year period, the information will be available for public release.**

---

---

Research sponsored by the U.S. Department of Energy, Assistant Secretary for Energy Efficiency and Renewable Energy, Office of Transportation Technologies, as part of the Heavy Vehicle Propulsion System Materials Program, under contract DE-AC05-96OR22464 with UT-Battelle LLC.

## INTRODUCTION

### Background

The development of new and improved ceramic materials, design methods for brittle materials, and life prediction methodology is of vital importance to the successful utilization of structural ceramics in advanced heat engine applications for transportation applications. In order to address these issues on an international level, a cooperative research agreement was initiated by several countries under the International Energy Agency (IEA). The original effort was started in 1979 through an Implementing Agreement for a Program of R&D on High-Temperature Materials for Automotive Engines. This agreement was completed in FY 1985, with DOE serving as Operating Agent for the United States. In this first agreement entitled, "Annex I-Ceramics for Automotive Gas Turbine Engines," the United States and Germany conducted information exchange and experimental ceramic materials and test results on those materials via participation of industrial and government laboratories in both countries.

Annex II, the current IEA agreement under which this international research is conducted, was started in 1985. The current participants are Germany, United States, Sweden, Japan, and Belgium. The United States Department of Energy is the Chairman of the Executive Committee and Operating Agent for Annex II. The active subtasks are (1) Subtask 9 - Thermal Shock Testing of Advanced Ceramics and (2) Subtask 10 - Characterization of Ceramic Powders. The purpose of Subtask 9 is to assess advanced techniques for the measurement of thermal shock of silicon nitride and other structural ceramics. The objectives of Subtask 10 are to (1) tighten and finalize procedures for characterization of secondary properties of selected powders; (2) delineate interrelationships between primary and secondary properties; and (3) unify IEA efforts with those of ASTM, CEN, and JIS—leading to ISO adaptation.

This report summarizes the Subtask 11 research activities, which involved participation from Germany, Japan, and the United States. The primary objective of this effort was to develop and verify techniques for the measurement of thermal and mechanical fatigue of structural ceramics. National efforts in Japan and the United States focussed on the development of procedures for evaluating the mechanical fatigue behaviour of silicon nitride ceramics using either uniaxial flexure or biaxial test specimens. The national effort in Germany consisted of the development of thermal fatigue procedures using the laser thermal shock equipment evaluated in Subtask 9 [1].

Subtask 11 also included an international effort in which the thermal and mechanical fatigue behaviors of two silicon nitride ceramics were compared with the mechanical fatigue data generated at a temperature which is the same as that at the fracture point in thermal fatigue test. Germany was responsible for the thermal fatigue testing while both Japan and the United States conducted mechanical fatigue testing.

This report summarizes the results from the international effort. Because this effort focused primarily upon the measurement comparison of static, dynamic, and cyclic fatigue properties of a commercial silicon nitride, the section that follows provides a mathematical treatment of the three types of behavior.

## A Generalized Approach for Static, Dynamic, and Cyclic Fatigue

We start by assuming that for a given flaw size,  $a$ , the associated fracture strength,  $S$ , is given as,

$$Y S (a)^{1/2} = K_{IC} , \quad (1)$$

where  $Y$  is a constant and  $K_{IC}$  is the fracture toughness. More generally when the applied stress,  $\sigma$ , is less than the fracture strength, Equation 1 becomes

$$Y \sigma (a)^{1/2} = K_I, \quad (2)$$

where  $K_I$  is the stress intensity factor. When slow crack occurs the crack length increases in accordance with power law equation,

$$da/dt = V = A K_I^N, \quad (3)$$

where  $A$  and  $N$  are constants,  $V$  is the crack velocity,  $t$  is time, and  $K_I$  is the stress intensity factor. The  $K_I$  term in Equations 2 and 3 can be eliminating yielding the expression,

$$da/dt = V = A (Y \sigma (a)^{1/2})^N, \quad (4a)$$

or

$$da/(a)^{N/2} = A (Y \sigma)^N dt. \quad (4b)$$

After integrating each side one has that

$$[(a_f)^{-N/2+1} - (a_i)^{-N/2+1}] / (-N/2+1) = A Y^N \int \sigma^N dt \quad (5a)$$

or after rearrangement

$$[(a_i)^{-N/2+1} - (a_f)^{-N/2+1}] = (N - 2)/2 A Y^N \int \sigma^N dt, \quad (5b)$$

where  $a_i$  and  $a_f$  are the initial and final crack lengths, respectively. These crack lengths can be related to the fracture strengths as follows

$$Y S_i (a_i)^{1/2} = K_{IC}, \quad (6a)$$

and

$$Y S_f (a_f)^{1/2} = K_{IC}. \quad (6b)$$

where  $S_i$  is the inert strength and  $S_f$  is the strength after time,  $t$ . Consequently, Equation 5 can be rewritten as

$$[(Y S_i / K_{IC})^{N-2} - (Y S_f / K_{IC})^{N-2}] = (N - 2)/2 A Y^N \int \sigma^N dt \quad (7a)$$

or

$$[(S_i)^{N-2} - (S_f)^{N-2}] = (N - 2)/2 A (K_{IC})^{N-2} Y^2 \int \sigma^N dt. \quad (7b)$$

or

$$[1 - (S_f / S_i)^{N-2}] = (N - 2)/2 A (K_{IC})^N (K_{IC}/S_i)^{-2} Y^2 \int (\sigma/S_i)^N dt. \quad (7c)$$

or

$$[1 - (S_f/S_i)^{N-2}] = (N - 2)/2 V(K_{IC}) (Y S_i/K_{IC})^2 \int (\sigma/S_i)^N dt. \quad (7d)$$

or

$$[(S_i)^{N-2} - (S_f)^{N-2}] / [(S_o)^{N-2}] = (N - 2)/2 V(K_{IC}) (Y S_o/K_{IC})^2 \int (\sigma/S_o)^N dt. \quad (7e)$$

where we have used the fact that  $V(K_{IC}) = A K_{IC}^N$ .

If the stress is constant, the integral on the right hand side of Equation 7b is  $\sigma^N t$ , yielding the following expression,

$$[(S_i)^{N-2} - (S_f)^{N-2}] = (N - 2)/2 A (K_{IC})^{N-2} Y^2 \sigma^N t. \quad (8a)$$

or

$$[1 - (S_f/S_i)^{N-2}] = (N - 2)/2 V(K_{IC}) (Y S_i/K_{IC})^2 (\sigma/S_i)^N t. \quad (8b)$$

In this case failure occurs when  $S_f = \sigma$ . For a constant stressing rate,  $d\sigma/dt$ ,  $\sigma = (d\sigma/dt) t$  and Equation 7b becomes:

or

$$[(S_i)^{N-2} - (S_f)^{N-2}] = [(N-2)/(2(N+1))] A Y^2 (K_{IC})^{N-2} (d\sigma/dt)^N t^{N+1}. \quad (9a)$$

or

$$[1 - (S_f/S_i)^{N-2}] = [(N-2)/(2(N+1))] V(K_{IC}) (Y S_i/K_{IC})^2 (S_i)^{-N} (\sigma)^{N+1} (d\sigma/dt)^{-1}. \quad (9b)$$

or

$$[1 - (S_f/S_i)^{N-2}] = [(N-2)/(2(N+1))] V(K_{IC}) (Y S_i/K_{IC})^2 (\tilde{\sigma} S_i)^N t. \quad (9c)$$

or

$$[1 - (S_f/S_i)^{N-2}] = [1/(N+1)] [(N-2)/2] V(K_{IC}) (Y S_i/K_{IC})^2 (\tilde{\sigma} S_i)^N t. \quad (9d)$$

For cyclic loading the applied stress is a periodic function of time ( $\sigma = \sigma_{max} f(t)$ ) such that

$$\int (\sigma/S_i)^N dt = (\sigma_{max}/S_i)^N (\tau N_{cyc}) [(1/\tau)]^{\tau} \int f(t)^N dt = (\sigma_{max}/S_i)^N (\tau N_{cyc}) I_{cyc}. \quad (10)$$

where  $N_{cyc}$  is the number of cycles and  $I_{cyc}$  is the value of the integral represented in brackets. Note that we have integrated the expression over one cycle (with period  $\tau$ ). When  $t \gg \tau$ ,  $N_{cyc}$  is approximated by the quantity  $t/\tau$ . The expression for time-dependent strength becomes

$$[1 - (S_f/S_i)^{N-2}] = (N - 2)/2 V(K_{IC}) (Y S_i/K_{IC})^2 (\sigma_{max}/S_i)^N (\tau N_{cyc}) I_{cyc}. \quad (11)$$

Note that for static loading  $\sigma = \sigma_{max}$ ,  $t = \tau N_{cyc}$ , and  $I_{cyc} = 1$  such that Equation 11 becomes identical to equation 8b.

## EXPERIMENTAL PROCEDURE

### Materials

The materials examined in this program were fabricated from either SN282 (Kyocera Ceramic Components in Vancouver, WA) or GS44 (Honeywell Ceramic Components in Torrance, CA)

silicon nitride. The SN282, which is densified by gas pressure sintering using rare-earth sintering aids, is classified as self-reinforced due the development acicular  $\beta$  silicon nitride grains. The crystalline phases in the as-received material are  $\beta$ -  $\text{Si}_3\text{N}_4$ ,  $\text{Lu}_2\text{Si}_2\text{O}_7$ , and  $\text{Lu}_2\text{SiO}_5$ . The GS44 material is cold isostatically pressed (CIPed) and then gas pressure sintered using 4 w/o  $\text{Y}_2\text{O}_3$  and 4 w/o spinel ( $\text{MgAl}_2\text{O}_4$ ) as densification aids. The resulting intergranular phase in the sintered material tends to amorphous in nature. Typical mechanical properties for these two materials are provided in Table 1 while microstructures are shown in Figure 1..

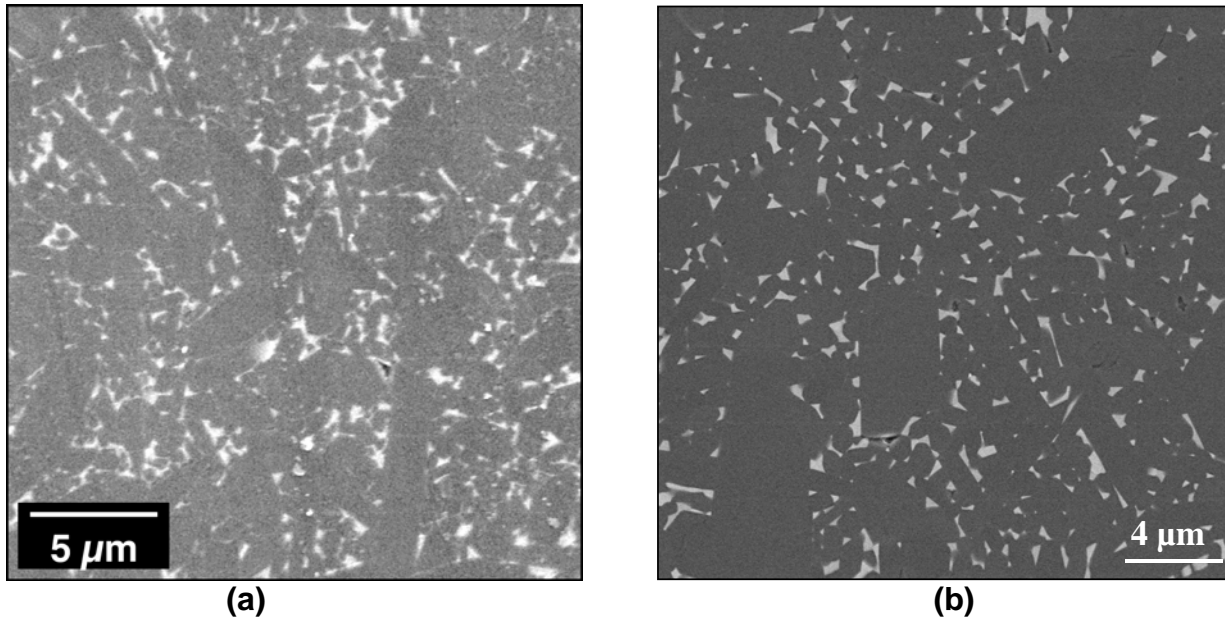


**Figure 1: Typical microstructures for (a) GS44 and (b) SN282 silicon nitrides.**

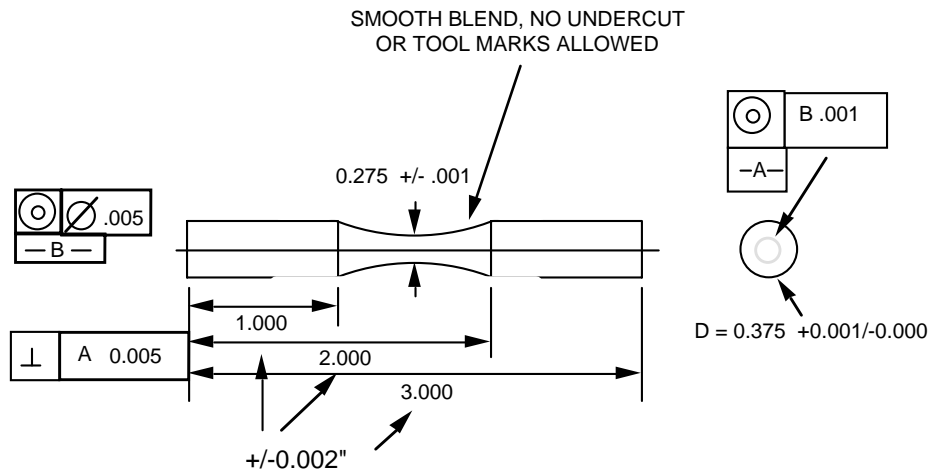
Table 1: Summary of mechanical properties for the GS44 and SN282 silicon nitride ceramics.

Material	FLEXURE STRENGTH (MPa)			FRACTURE Toughness (MPa $\sqrt{\text{m}}$ )	Weilbull Modulus
	25°C Machined	25°C as-Sintered	1260°C Machined		
SN282	729	648	705	4.5	10-30
GS44	935	NA	NA	8.2	20-30

### Test Conditions-United States

Two types of test specimens were machined from the as-received billets of the GS44. The first was Size B flexure bars with nominal dimensions of 3 by 4 by 50 mm. These specimens were used for both static and dynamic fatigue testing (described below). The second specimen type was a cylindrical dog-bone specimen (Figure 2) used for the rotary bend fatigue (RBF) tests.

The static and dynamic fatigue tests were conducted the Flexure Test System (FTS), which provides for the application of selected load-time profiles to flexure, compression, c-ring, and o-ring specimens at elevated temperatures (Figure 3). A maximum of three specimens can be simultaneously tested at temperatures up to 1600°C. The loads are generated by pneumatically-



- SURFACE FINISH  $0.4 \mu\text{m}$  ALL OVER
- FINAL GRIND OF GAGE SECTION TO BE TRANSVERSELY MACHINED
- MATERIAL: 95 %  $\text{Al}_2\text{O}_3$  (SUPPLIED)
- ALL DIMENSIONS IN INCHES
- NOTE: RUNOUT CAN NOT EXCEED .002"

Figure 2: Rotary bend fatigue specimen.

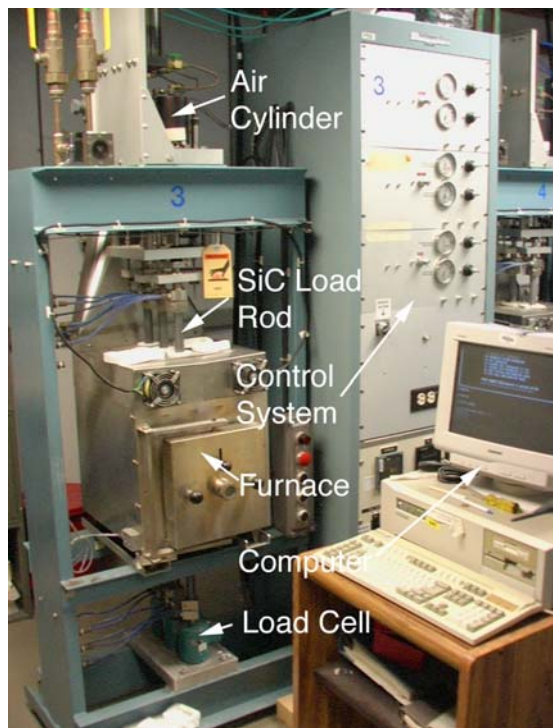


Figure 3: Key components of Flexure Tests System.

driven air cylinders located at the top of the support frame. In order to minimize impact problems normally encountered during fracture, a hydraulic fluid is used as the working medium in the cylinder. The cylinder pressure and thus, the applied load is controlled by an I/P transducer. The mechanical loads are transmitted into the hot zone of the furnace through SiC rods. Each of the bottom three SiC support rods is also attached to a load cell which monitors the applied force. Load-point displacement for each load train is determined by an SLVC, which is attached to the upper load rod. Finally, the temperature is monitored with a Type S thermocouple attached to the middle load rod.

A data acquisition system (DAS) is used to digitize the load cell, SLVC, and thermocouple signals as well as monitor various FTS status signals including furnace door interlock, water flow indicator, and fracture detection. In addition, the DAS provides three 4 to 20 MA outputs required to control the I/P transducers. The status of four solid state relays is also controlled by the DAS. Three of these relays are used to open and close solenoid valves located between the air cylinder and I/P transducer. The fourth solid state relay energizes the furnace relay, which provides power to the furnace elements.

For the current program static and dynamic fatigue tests were conducted at 850°C. For static fatigue testing, the applied stresses ranged from 400 to 750 MPa. Two stressing rates, 30 and 0.003 MPa/s, were used for the dynamic fatigue tests. Additional details are provided in [2].

The initial configuration of the rotary bend fatigue (RBF) machine being used for this effort is shown in Figure 4 while Figure 5 illustrates the loading configuration. Note that the dead weight loading that is normally used to generate stresses in the specimens was replaced by a computer controlled pneumatic loading system. This system could either maintain a static load or control the load as a function of time.

For the configuration in Figure 5, the maximum stress at the gage diameter is given by

$$S = M D / (2 I) \quad (12a)$$

$$M = P (L-x) \quad (12b)$$

$$I = \pi D^4 / 64 \quad (12c)$$

where S is the stress, M is the bending moment, D is the gage diameter, P is the applied load, I is the moment of inertia, L – x is the distance from the load point to the gage section. In order to verify the stresses predicted by Equations 12a-c, the strain was measured using a steel specimen having two diametrically opposed gages mounted in the gage section. Figure 6 compares the measured strain with that predicted from Equation 12a using an elastic modulus of 220 GPa. The fact the slope of the data is very close to 1 validates Equation 12.

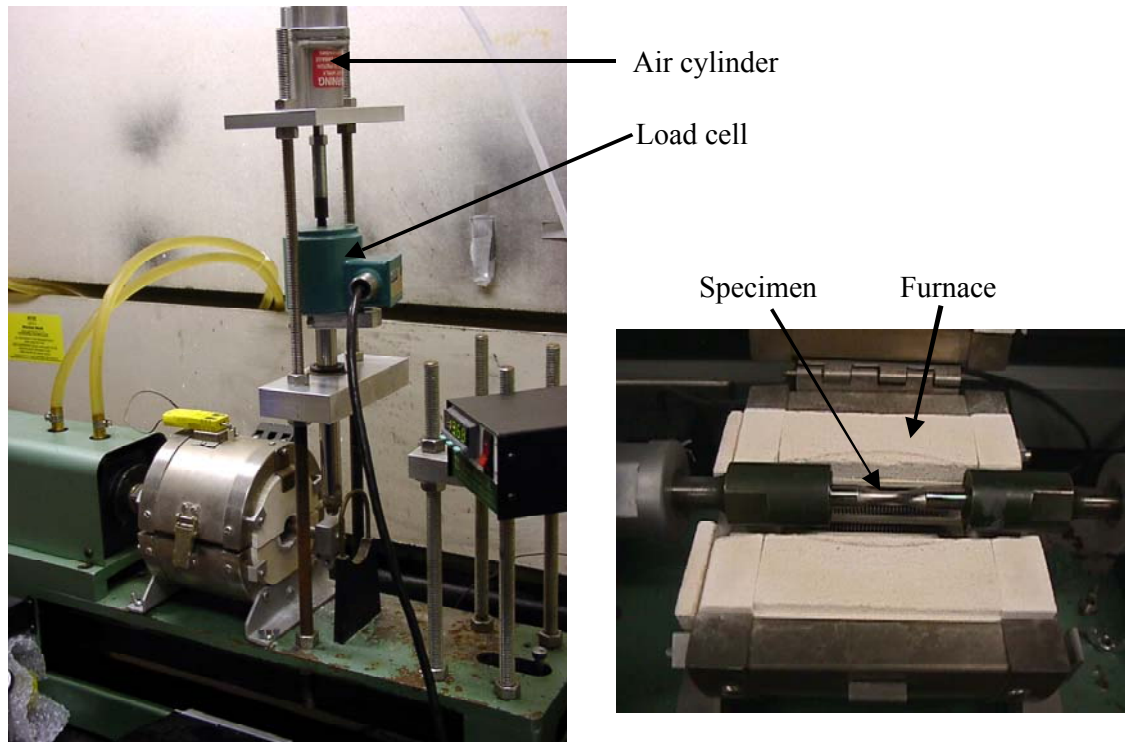


Figure 4: Rotary fatigue machine modified with computer-controlled pneumatic loading system.

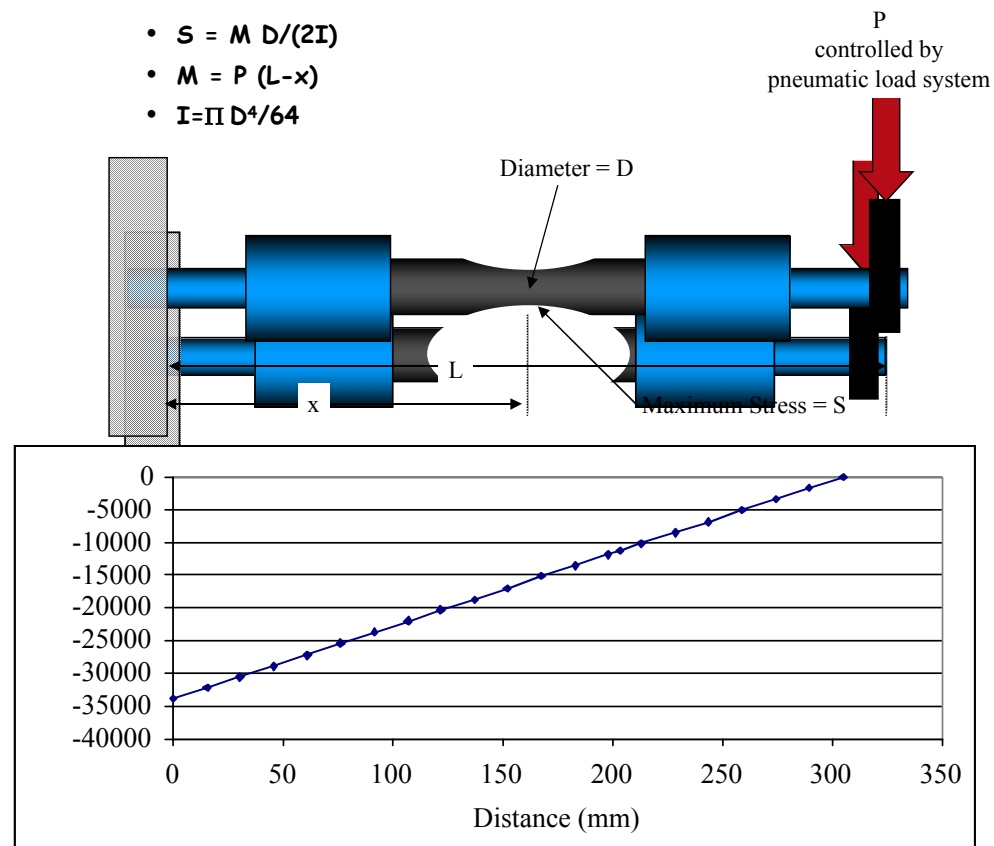


Figure 5: Schematic representation of the load geometry and corresponding moment diagram.

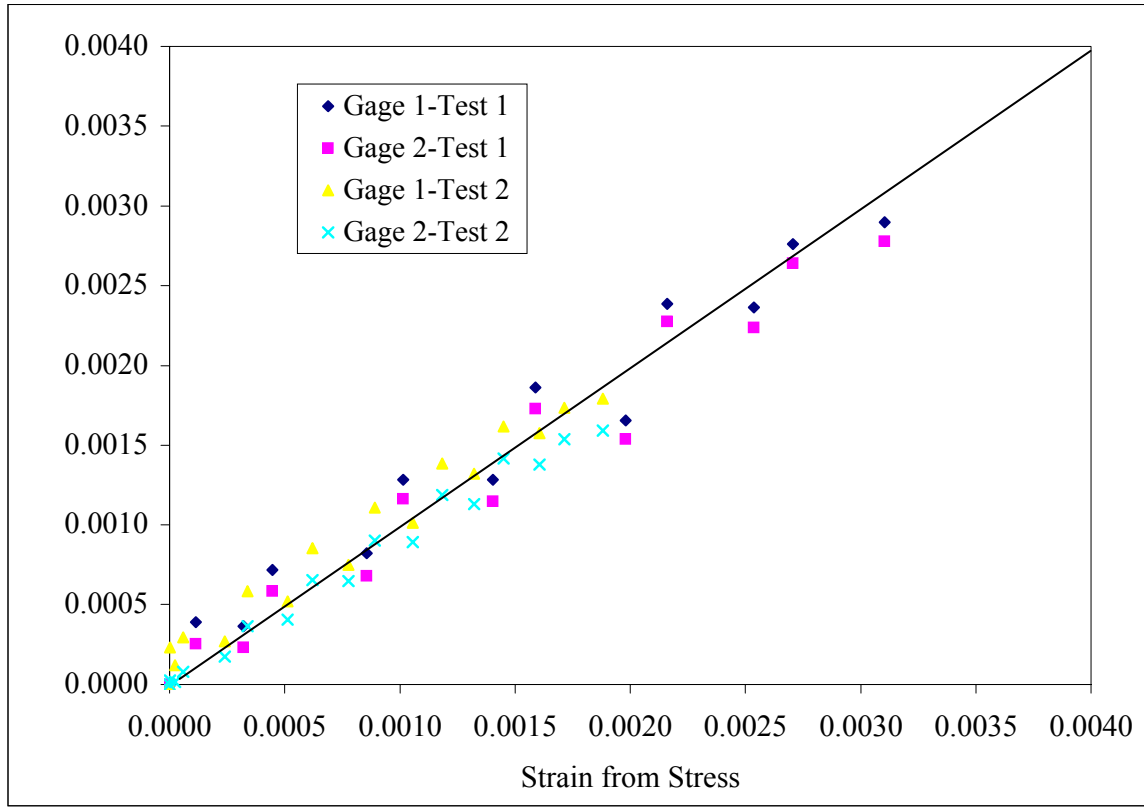


Figure 6: Comparison of measured strain with that predicted from Equation 12 for the experimental setup shown in Figures 4 and 5.

The RBF setup in Figures 4 and 5 was used to measure strength as a function temperature (700 and 850°C), stressing rate (0.0002 and 1.2 MPa/s), and rotational speed (0 and 1200 rpm). During slow loading rate tests, deformation of the left-hand grip<sup>1</sup> caused excessive deformation at the free end of the cantilever, which prevented the test from completing. This problem was attributed to the combined effects of high stresses<sup>2</sup> and temperatures in the left-hand grip, which caused the metal collets to creep. The application of several grip cooling and insulation schemes did not solve the problem. In an attempt to reduce the stresses in the vicinity of the left-hand grip, an opposing loading configuration was developed (Figure 7). For this load geometry,  $M$  is given by

$$M = (P_2 X_2 - P_1 X_1) - X (P_2 - P_1) \text{ (for } X < X_1) \quad (13)$$

where the  $P$ s represent loads and the  $X$ s are the distances from the fixed end (Figure 7). When  $P_2 = P_1$ , the moment for is independent of  $X$  as shown by the moment diagram in Figure 7. The

<sup>1</sup> This is the grip closest to fixed end of the cantilever.

<sup>2</sup> Note that the stresses in the left-hand grip are higher than those in the right-hand grip due to the higher bending moment.

stress is still given by Equation 12a. Subsequent strain measurements made with the gaged specimen were in good agreement with the strain values determined from the stress (Figure 8).

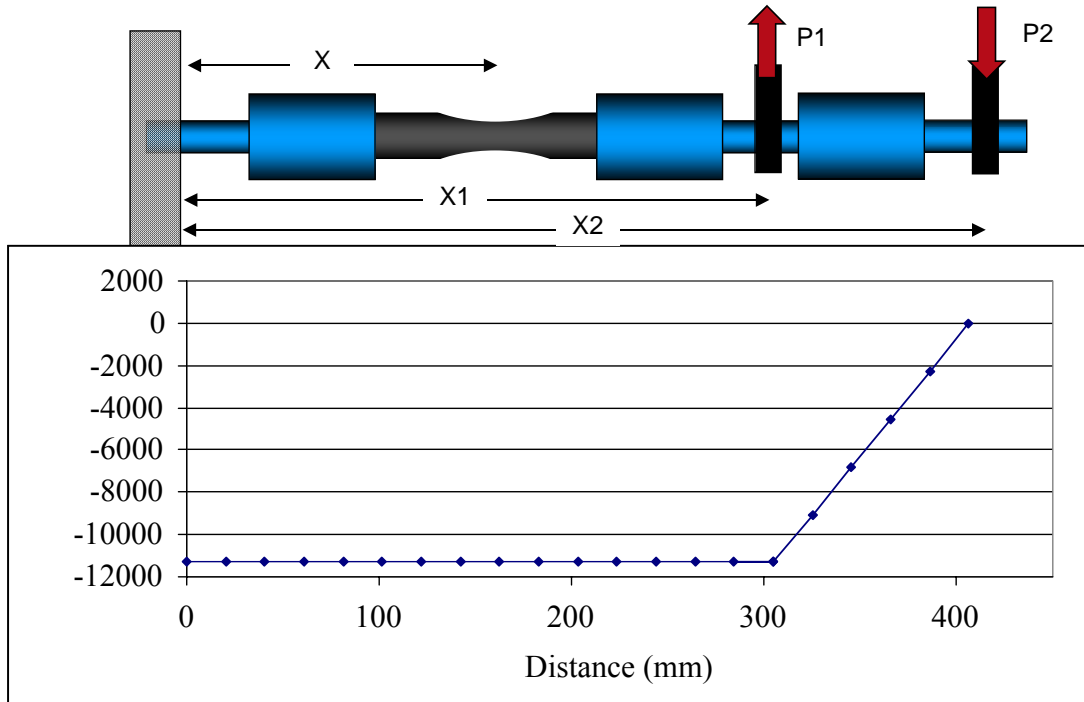


Figure 7: Schematic representation of the opposing load geometry and corresponding moment diagram.

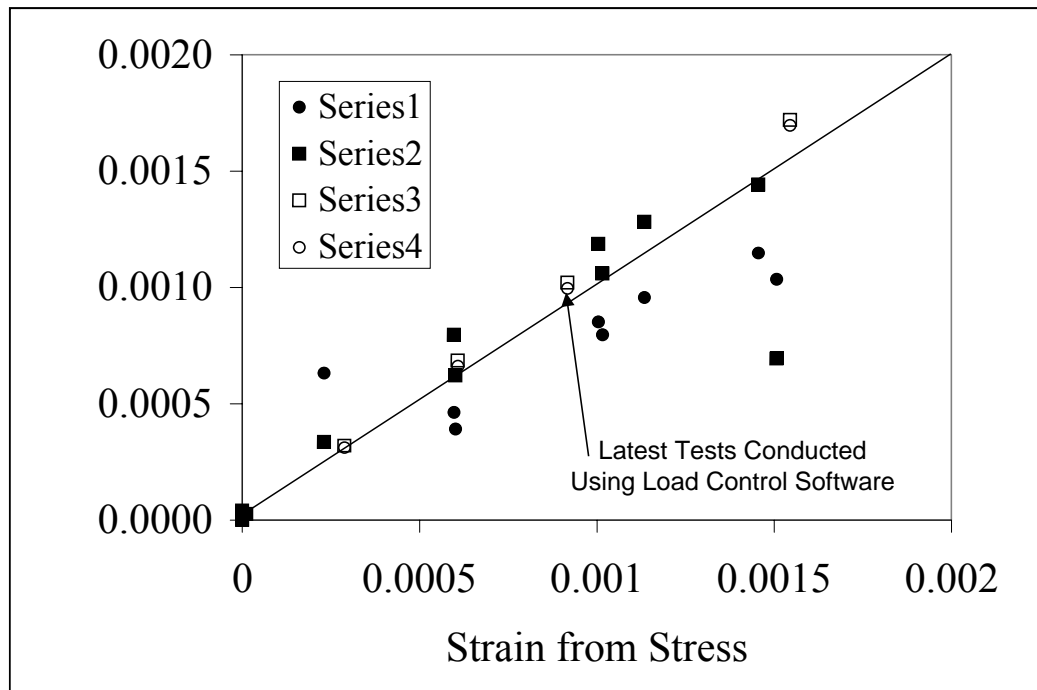


Figure 8: Comparison of measured strain with that predicted from Equations 1a and 2 for the experimental setup shown in Figure 7. The scatter in Series 1 and 2 was due to load fluctuations. Series 3 and 4 were conducted using improved load-control software.

### Test Conditions-Japan

Fifteen 3 by 4 by 50 mm flexure bars of SN282 and 34 bars of GS44 were used for the evaluation of strength and uniaxial bending fatigue. A limited number of flexural strength tests were conducted on these specimens in order to determine a testing stress for the fatigue tests. Subsequent bending fatigue tests were conducted at room and elevated temperatures in air using a servo-hydraulic testing system (Model Servo Pulsar EHF-FD1). The inner and outer spans for these tests were 20 and 40 mm, respectively. The fatigue tests were carried out with a sinusoidal loading frequency of 20 Hz or 1 Hz in air. The stress ratio, which is defined as the ratio of minimum stress to maximum stress, was 0.1. The run out limit on the number of cycles was set to  $10^7$ . The fixture was made of silicon carbide. These testing conditions are based on the JIS standard [3].

As shown in Table 2, the maximum stresses for the fatigue tests of SN282 at 850°C were 95, 90, 85, and 80% of the average flexural strength. The maximum stresses for the fatigue tests of GS44 were 95, 90, 85, and 80% of the average flexural strength at 850°C and 97.5 and 95% at 1000°C.

Table 2: Test conditions for flexural & fatigue tests and number of specimens per condition.

Material	Flexural Strength T °C	Fatigue Test T °C/% Stress	Number Tested	
SN282	850		3	
		850/95%	2	
		850/90%	2	
		850/85%	2	
		850/80%	2	
GS44	RT		3	
		850	3	
	850	850/95%	3	
		850/90%	3	
		850/85%	3	
		850/80%	3	
		1000		3
			1000/95%	3
			1000/97.50%	3

### Test Conditions-Germany

The setup used for the thermal fatigue tests was based on the thermal up-shock technique [4] in which a disk specimen is centrally heated to fracture by an appropriate heating source. As shown in Figure 9, heating was achieved by using a Nd: YAG - laser (1064 nm and 1200 W cw max) to irradiate the specimen in a spiral pattern, which originated at the specimen center and extended outward covering a region 16 to 16.5 mm in diameter region. To insure sufficient coverage and minimum heating time, the spacing between successive spirals was 0.3 - 0.5 mm and the maximum heating time was 0.5 to 0.8 s. The laser power necessary for thermal shock fracture of the silicon nitride ceramics was in the range of 700 - 1000 W.

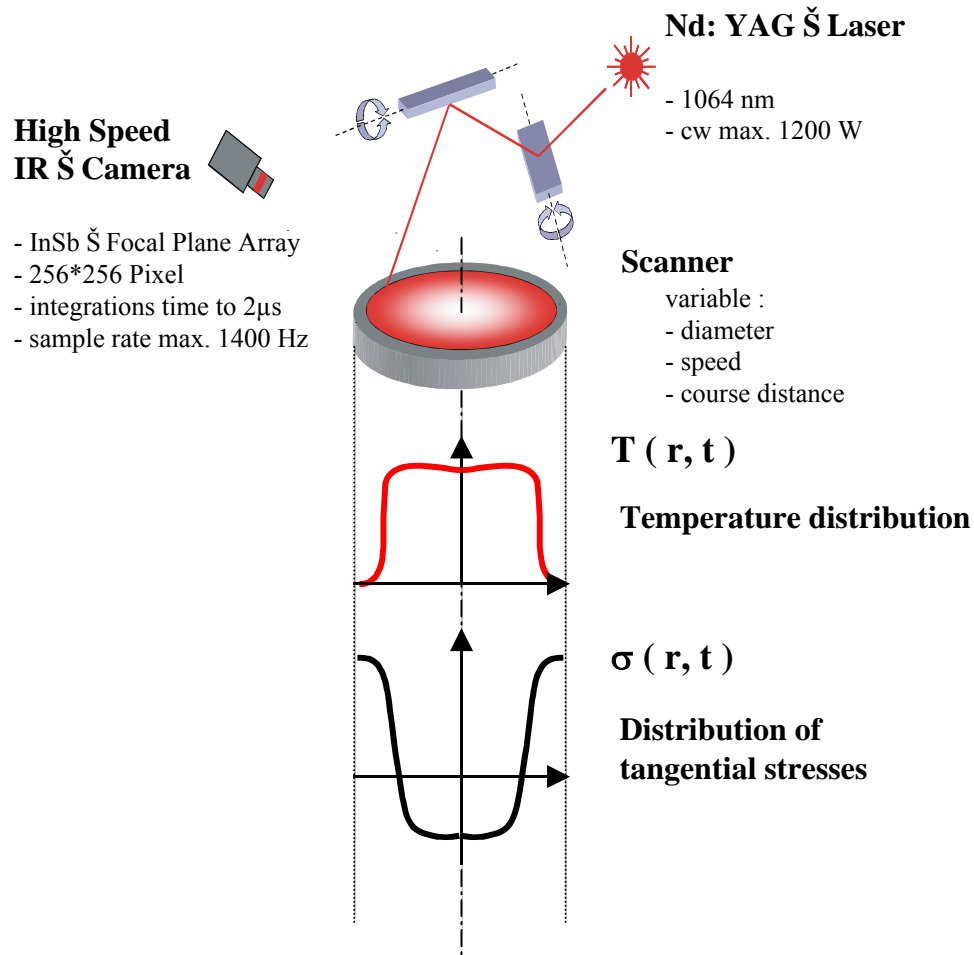


Figure 9: Set-up used for thermal shock and thermal fatigue tests.

A high-speed infrared camera employing a InSb - focal plane 256\*256 pixel array was used to measure the temperature distribution as a function of time. The maximum sampling rate was 1400 Hz. A special procedure was required correct for the inaccuracy in the temperature readings at the sample rim. Specifically the IR camera tended to overestimate the temperatures in this area. The correction involved assuming that the temperature at the outer edge was 25°C and then extrapolating the temperature profile to this value.

All specimens were 20 mm in diameter and 0.3 mm in thickness. Prior to testing each specimen was cleaned in ethanol in the ultrasonic bath for 15 min. Preliminary studies focused on the measurement of the thermal shock properties of the SN282 and GS44.

Next attempts were made to control the laser power as function of time such that the thermal fatigue behavior could be assessed. Unfortunately it was not possible to optimize the control parameters such that the specimens failed in a consistent fashion under thermal cycling conditions.

## RESULTS AND DISCUSSION

### Static Fatigue-United States

The static fatigue data measured at 850°C using the GS44 flexure specimens are shown in Figure 10. As discussed in [2], the susceptibility of GS44 to time-dependent loss in strength was much greater at this temperature than that observed at temperatures <700°C. The associated strength degradation mechanism was attributed to softening of the intergranular phases, which ultimately led to viscous flow and separation of grain facets. Given sufficient time, this viscous flow was ultimately responsible for the formation of cavities within the intergranular phase. For example, Figure 11 compares the fracture surfaces of two dynamic fatigue specimens; one tested at 30 MPa/s and other at 0.003 MPa/s. At 0.003 MPa/s there was sufficient time for the cavitation to occur as evidenced by the skeletal pattern of the intergranular phase outlining the interfaces between adjacent grains. It should be noted that similar behavior was observed for a hot-isostatically pressed silicon nitride when tested under tensile loading at temperatures above 1200°C [5]. In that study, however, the temperatures were sufficiently high to activated addition deformation mechanisms including cavitation of the silicon nitride by a solution-precipitation process.

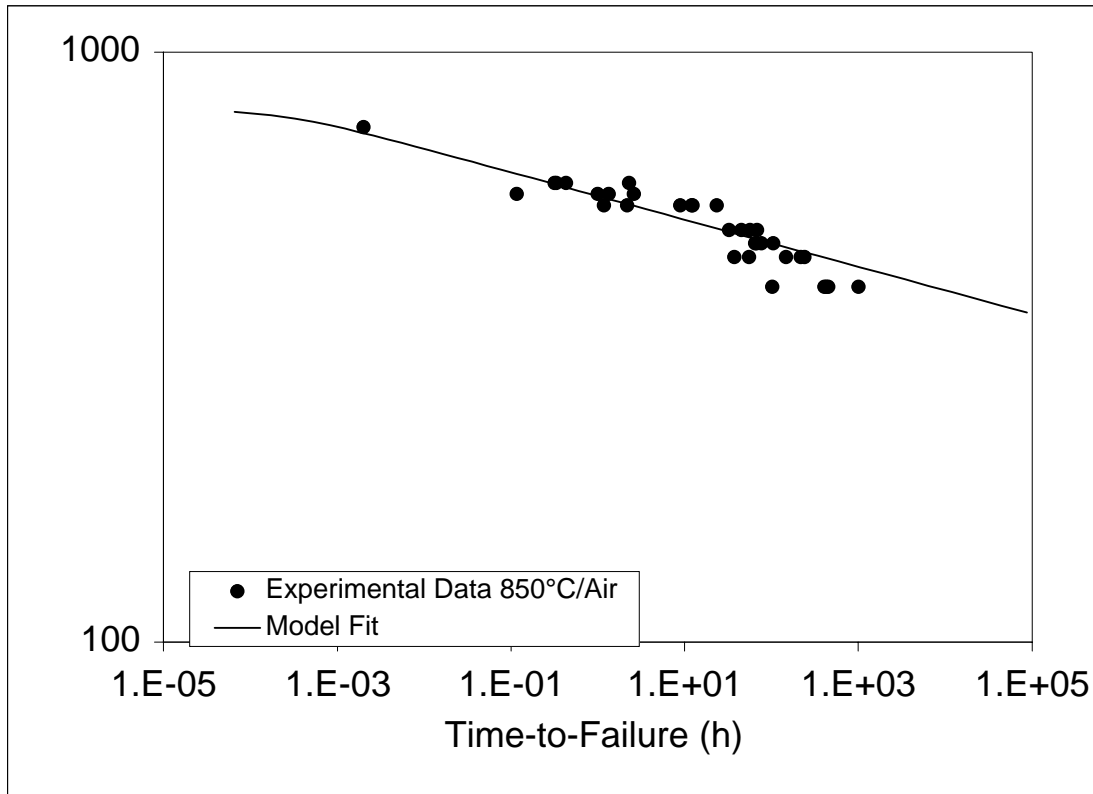


Figure 10: Flexural static fatigue data generated at 850°C. The symbols represent the experimental data while the solid line is the fit of these data to Equation 8.

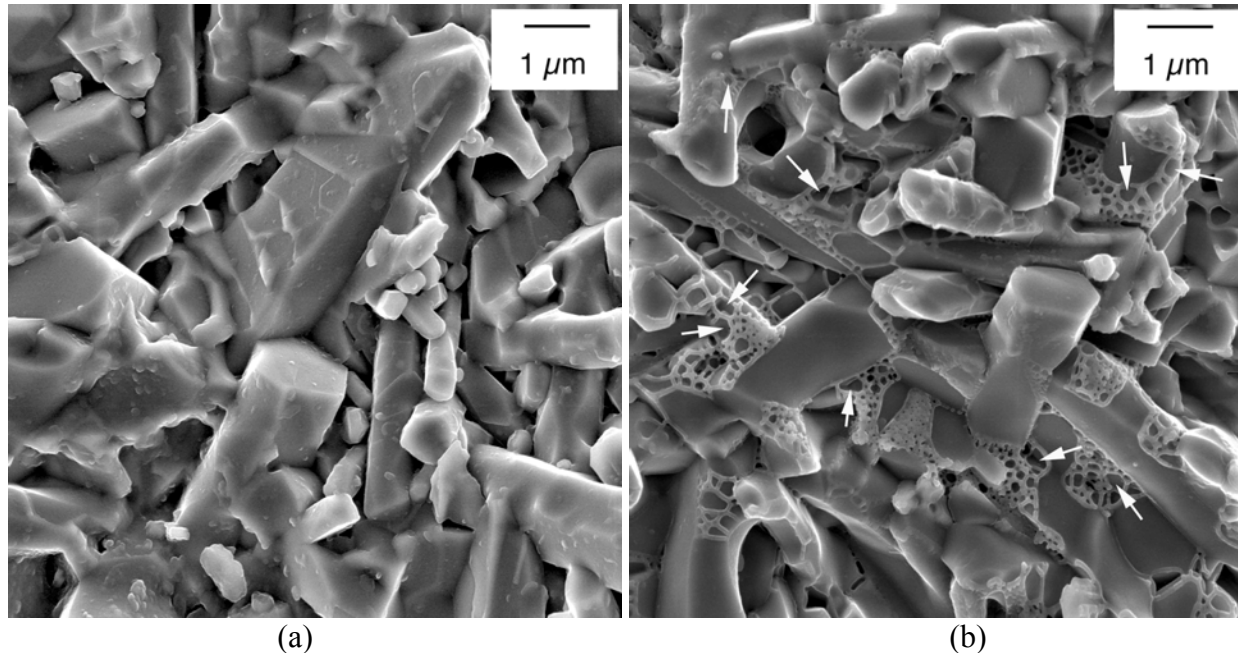


Figure 11: Comparison of fracture surfaces of two flexure specimens tested at (a) 30 MPa/s and (b) 0.003 MPa/s. The test temperature was 850°C.

The experimental static fatigue data were subsequently fit to Equation 8 by choosing values of  $S_i$ ,  $N$ , and  $V(K_{IC})$  which minimized the sum of the square of errors between predicted and measured lifetimes. The fracture toughness at 850°C was assumed to be comparable to the room-temperature value reported by the vendor ( $8 \text{ MPa m}^{1/2}$ ). The resulting values of the crack growth parameters estimated using this iterative procedure are provided in Table 3. The solid line in Figure 10 illustrates the model prediction. Note that the value of  $V(K_{IC})$  is relatively low. One might expect that it should be comparable to the speed of sound given that it associated catastrophic fracture. However, this parameter actually represents the velocity occurring at the intersection of the Region I slow crack growth curve with Region III curve as shown schematically in Figure 12. Because the Region III crack growth makes very little contribution to the time-dependent failure, it is treated as a vertical line in the development of the equations describing static, dynamic, and cyclic fatigue.<sup>3</sup>

Table 3: Crack growth parameters.

Parameter	Value	Comments
Y	1.5	Based on surface cracks
$K_{IC}$ (MPa $\text{m}^{1/2}$ )	8	Based on vendors information
$V(K_{IC})$ (m/s)	$5 \times 10^{-6}$	
$S_i$ (MPa)	800	
N	25	

<sup>3</sup> The contribution of Region II slow crack growth to time-dependent failure is also ignored.

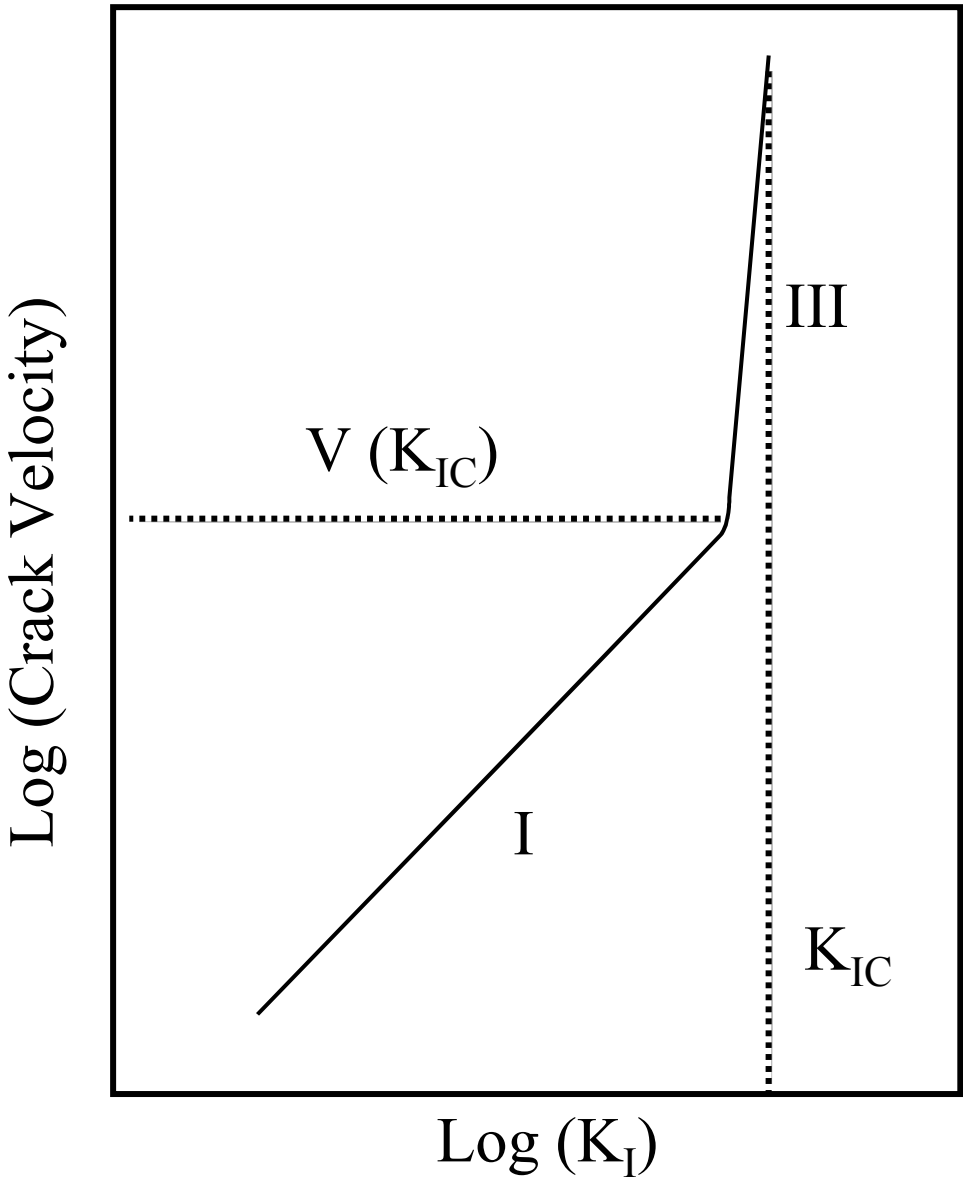


Figure 12: schematic representation of V-K<sub>I</sub> behavior showing two regions of crack growth. Because the slope of Region III is very high, its contribution to time-dependent failure can be neglected. In this case, V (K<sub>IC</sub>) represented the intersection of the Regions I and III curves.

**Dynamic Fatigue-United States**

Figure 13 illustrates the results of the dynamic fatigue testing conducted at 850°C. The slow crack growth exponent, N, can be estimated from these data using the simplified form of Equation 9b:

$$(d\sigma/dt) = [(N-2)/(2(N+1))] V(K_{IC}) (Y S_i/K_{IC})^2 (S_i)^{-N} (\sigma)^{N+1}. \tag{14}$$

In this case N+1 is equal to the slope of strength-stressing rate plot. Using this method for the data in Figure 13, N was estimated as 33.

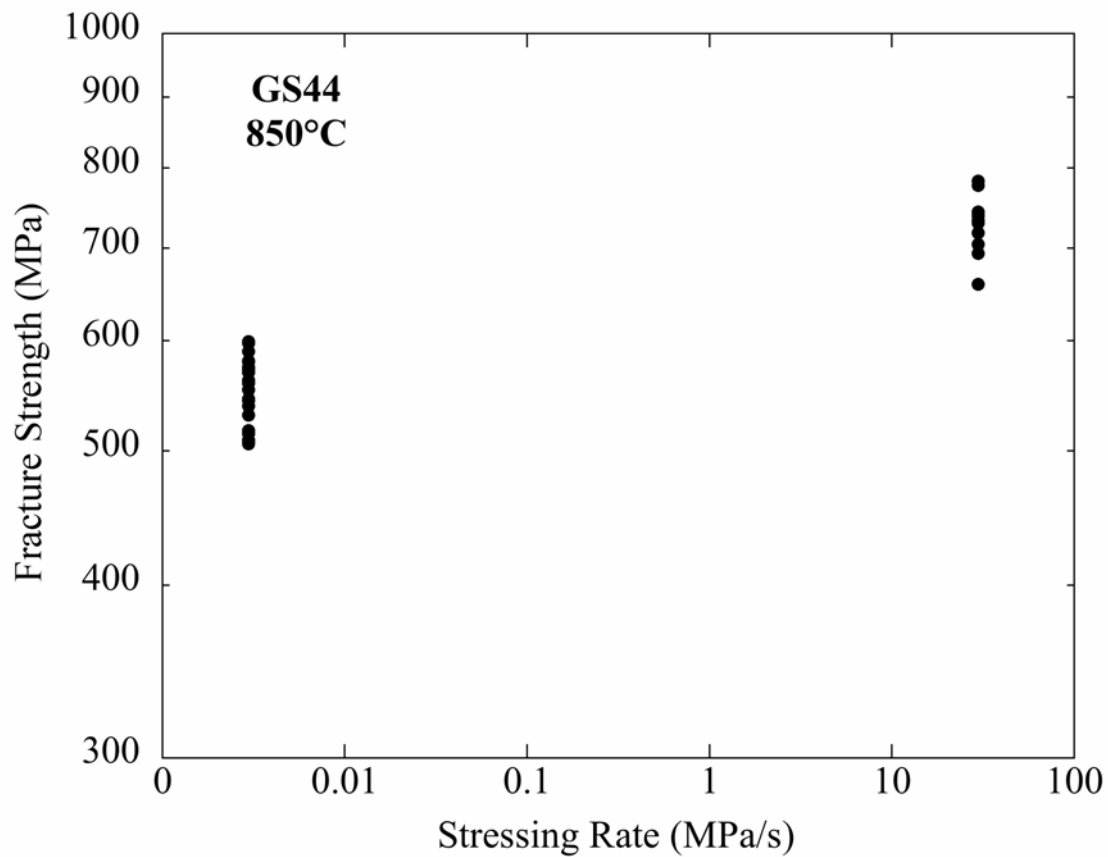


Figure 13: Strength versus stressing rate data for the GS44 material.

### Cyclic Fatigue-Japan

The average flexural strength and standard deviation of the SN282 at 850 °C in air were 562 and 57.3 MPa, respectively. It is noted that only three specimens were tested due to the limited number of specimens. Therefore, the average value is subject to considerable uncertainty. Flexural fatigue data of SN282 at 850 °C in air are shown in Table 4 and Figure 14. For the testing stresses of 95, 90, 85, and 80% of the average flexural strength, specimens fractured just after loading (less than 2.3 seconds; 46 cycles). One specimen, tested at a stress of 80%, did not fracture up to loading cycles of  $10^7$ . Therefore SN282 at 850 °C in air shows an on-off behavior and did not show fatigue behavior.

The average flexural strengths of GS44 at room temperature, 850 °C, and 1000°C in air were 805, 698, and 497MPa with standard deviations of 81.2, 71.2, and 50.7, respectively. Once again due to the limited number of specimens, only three specimens were tested at each temperature. The fact that the strength at 1000°C was about 62% of that at room temperature could be attributed to the softening of the intergranular phase. It should be emphasized that the manufacturer stated use temperature of the GS44 1100°C or below.

Table 4: Flexural fatigue data of SN282 at 850 °C in air.

Specimen No.	Thickness (mm)	Width (mm)	Stress (MPa)	Cycles to Fracture	Time to Fracture (s)
SN282-4	2.962	4.004	533	1	0.05
SN282-5	2.994	4.004	533	1	0.05
SN282-6	2.973	4.003	505	1	0.05
SN282-7	2.992	4.009	505	1	0.05
SN282-8	2.976	4.002	477	1	0.05
SN282-9	3.014	4.005	477	26	1.3
SN282-10	2.975	4.004	449	46	2.3
SN282-11	2.993	3.997	449	10,000,000	500000

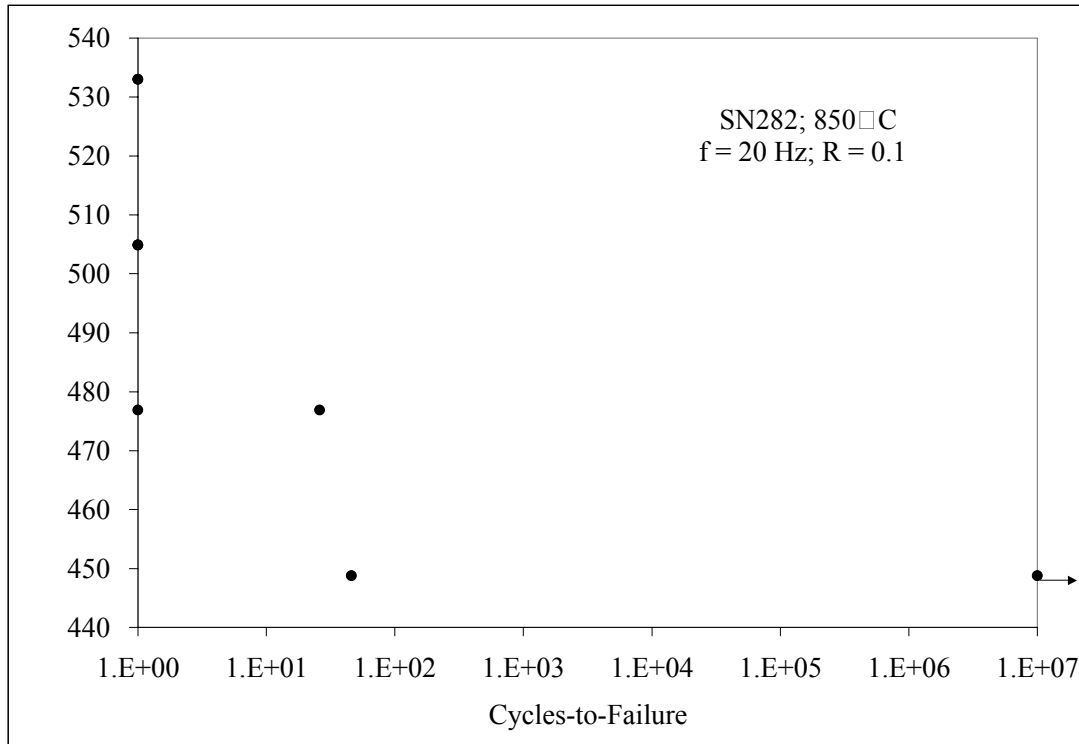


Figure 14: Flexural fatigue plot for SN282 at 850 °C in air.

Flexural fatigue data for the GS44 material were generated at 850 and 1000 °C in air (Table 5 and Figure 15). The fatigue data at 850°C showed a measurable fatigue effect. Although the number of cycles to failure showed some broad scatter at testing stresses of 95, 90, 85, or 80% of the average flexural strength, the number of cycles increased gradually with decreasing the stress. The fatigue coefficient calculated by the least square method was 42. On the other hand, GS44

did not fracture after  $10^7$  cycles loading at 1000 °C. The testing stress was 95 or 97.5 % of the average flexural strength, suggesting that at 1000°C the GS44 exhibits an on-off behavior. This phenomenon is probably due to the healing (or oxidation) of the specimen surface at 1000°C.

Table 5: Flexural fatigue data of GS44 in air.

Specimen No.	T (°C)	Thickness (mm)	Width (mm)	Stress (MPa)	Cycles to Fracture	Time to Fracture (s)
GS44-10	850	2.995	4.000	663	1,209,985	60499
GS44-11		2.996	3.995	663	93,090	4655
GS44-12		2.996	4.002	663	231,842	11592
GS44-13		2.995	3.997	628	496,319	24816
GS44-14		2.993	3.998	628	56,291	2815
GS44-15		2.991	3.998	628	205,101	10255
GS44-16		2.992	4.001	593	1,106,373	55319
GS44-17		2.991	3.998	593	77,363	3868
GS44-18		2.996	4.023	593	10,000,000	500000
GS44-19		3.012	4.020	558	1,108,893	55445
GS44-20		3.002	4.007	558	526,772	26339
GS44-21		2.999	4.001	558	5,768,694	288435
GS44-22	1000	3.004	4.015	472	10,000,000	500000
GS44-23		3.005	4.006	472	10,000,000	500000
GS44-24		3.005	4.005	472	10,000,000	500000
GS44-25		3.003	4.005	485	10,000,000	500000

### Cyclic Fatigue-United States

The preliminary RBF tests were conducted using the single load point configuration (Figure 5) at two stressing rates with no rotation applied to the specimen. The purpose of these tests was to determine if the resulting strength versus stressing rate data were comparable to those obtained from the flexure specimens. Figure 16 compares the dynamic fatigue data obtained for the two specimen types. It is clear that at the slower loading rate, the RBF specimens did not exhibit the same drop in strength as did the flexure specimens. Therefore the RBF data failed to predict the slow crack growth behavior of the GS44 silicon nitride. This behavior was attributed to creep of collets located in the grip at the fixed end, which caused excessive movement of the free end of the specimen at the slower loading rate. This in turn led to eventual contact of the specimen free end with the furnace insulation, which effectively lowered the gage section stress.

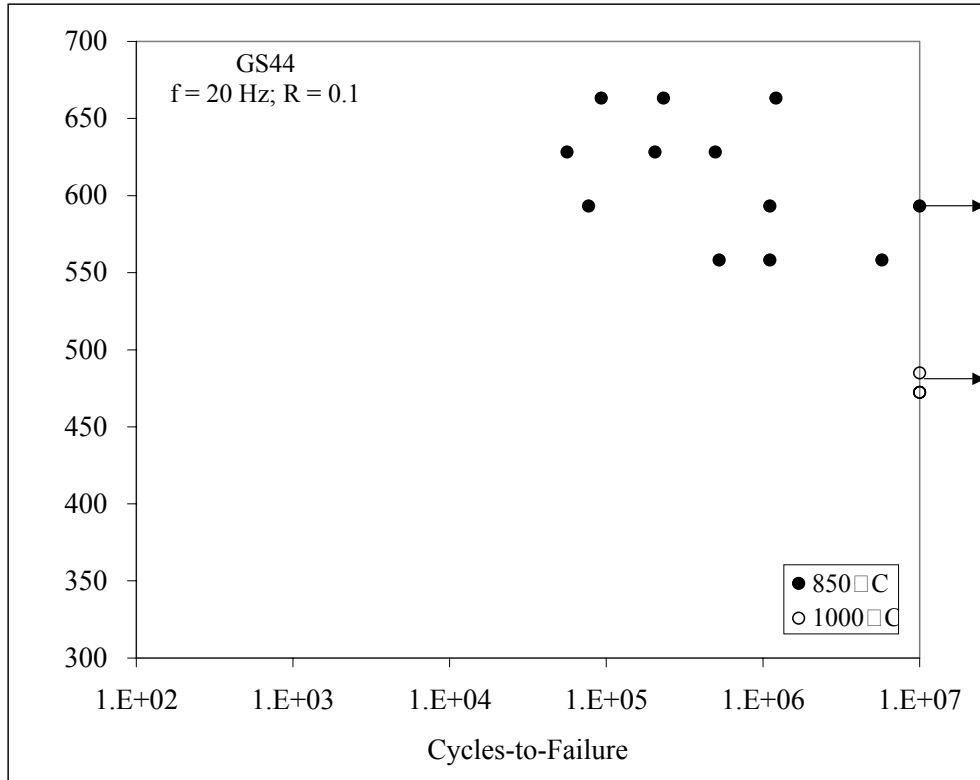


Figure 15: Flexural fatigue plots for GS44 at 850 and 1000°C in air.

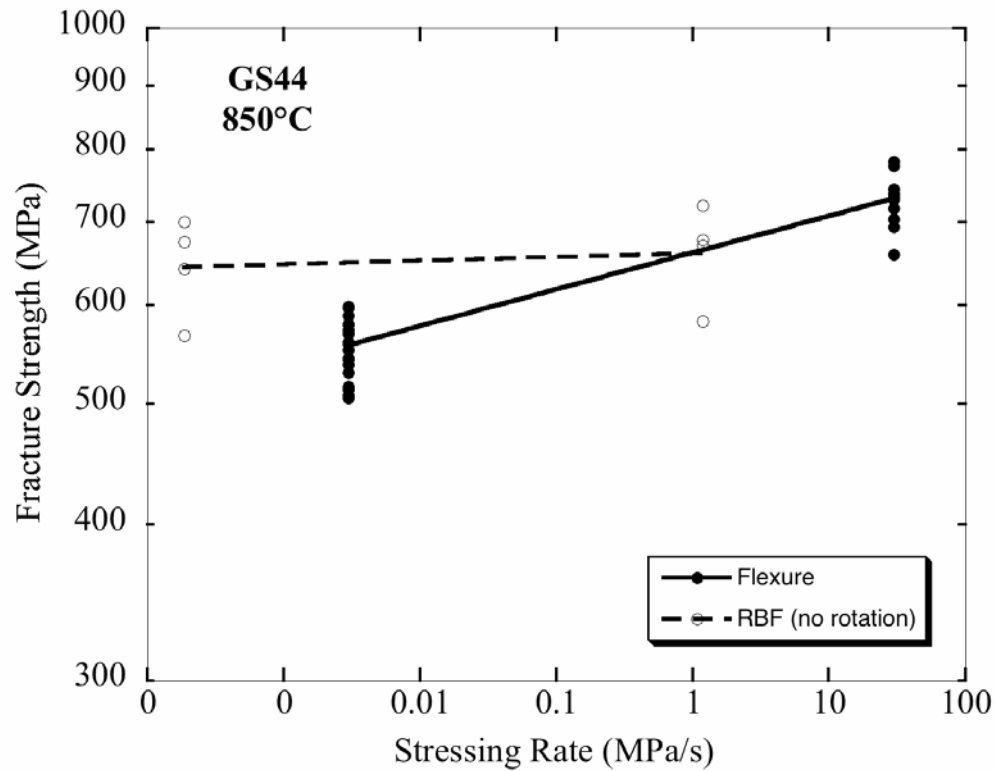


Figure 15: Comparison of dynamic fatigue results obtained from testing flexure and RBF specimens.

Although the use of the dual acting air cylinder system in Figure 7 resulted in a lower stress on the collets, creep was still a problem. In addition, the thermal expansion mismatch between the ceramic specimen and metal grip caused a reduction in the gripping forces during furnace heat-up, which prevented the specimen from turning during the RBF test. It was concluded that in order to avoid these problems a longer specimen would be necessary.

### **Comparison of Static, Dynamic, and Cyclic Fatigue**

As indicated by the various forms of Equation 9, different combinations of strength, stressing rate, and time-to-failure (strength/stressing rate) can be used to describe the dynamic fatigue data. As shown in Figure 16, the use of strength versus time-to-failure facilitates the direct comparison of static and dynamic fatigue results. Note that the experimental dynamic fatigue data points are shifted to longer times due to fact that in a dynamic fatigue test the stress is not constant but increases linearly from zero to final fracture strength. The same relationship is reflected by the predicted static and dynamic fatigue curves. In the latter case the curve was predicted from the static fatigue results by applying the slow crack growth parameters in Table 3 to Equation 9c. The agreement is quite good.

It is clear in Figure 16 that Equations 8 and 9 predict a stress (strength) plateau as the time approaches zero. In this regime, the static and dynamic fatigue behaviors are controlled primarily by Region III crack growth (Figure 12), which is assumed to be very steep. Often the effect of Region III is ignored in the development of the slow crack growth equations which leads to simplified versions of Equations 8 and 9 in which  $(S_f/S_i)^{N-2} \sim 0$ . This can lead to significant errors in the prediction of the crack growth parameters particularly if much of the data are obtained at short times. This explains why the N value determined from the application of Equation 14 to the dynamic fatigue data was significantly greater than that determined from the application of Equation 8 to the static fatigue data.

The data in Table 3 were also used in conjunction with Equation 11 to predict the cyclic fatigue results. In this case the value of  $I_{cyc} = [(1/\tau) \int_0^\tau f(t)^N dt]$  was evaluated for the sinusoidal waveform using numerical integration. The fact that the predicted dynamic and cyclic fatigue curves are in good agreement with the actual data suggests that at 850°C the slow crack model is indeed responsible for the time-dependent loss in strength for static, dynamic, and cyclic loading.

### **Thermal Shock**

The results of the thermal shock tests for the SN282 and the GS44 materials are shown as Weibull plots in Figure 18. The values of Weibull modulus (m) and characteristic strength ( $\sigma_c$ ) were similar for both materials: GS44 - m = 9 and  $\sigma_c = 410$  MPa and SN282 - m = 8 and  $\sigma_c = 378$  MPa. The average strengths were 387 +/- 50 and 364 +/- 44 MPa for the GS44 and SN282, respectively. A comparison of these results with the flexure strength-temperature data in Figure 19 reveals a number of important differences.<sup>4</sup> First based on the data in Figure 19 one would

---

<sup>4</sup> Given than thermal fracture occurs in the low temperature regime of the disk specimen, the relevant data in Figure 19 are those for  $T < 100^\circ\text{C}$ .

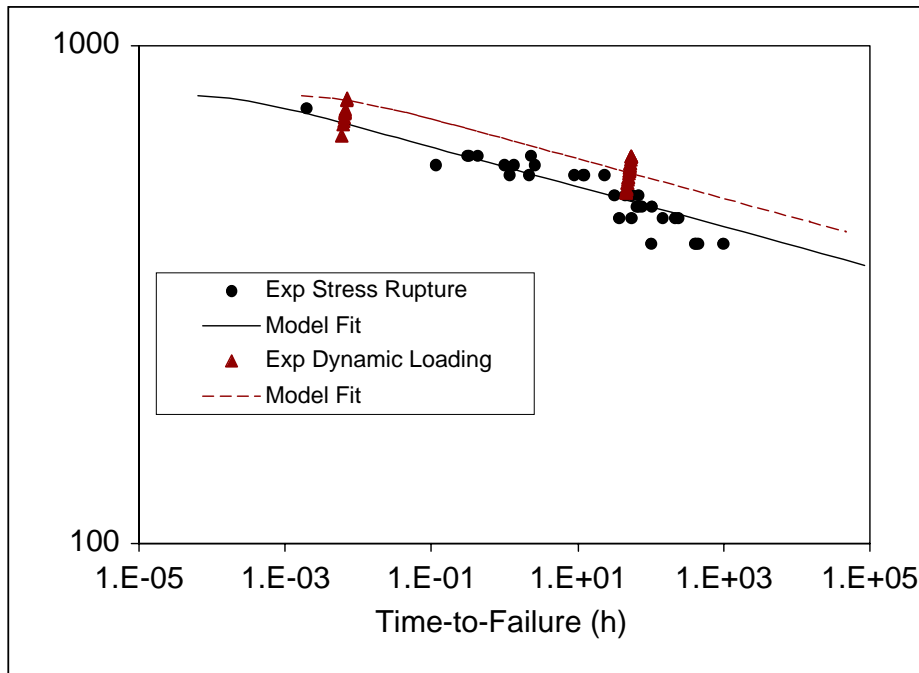


Figure 16: Comparison of static and dynamic fatigue results. The dynamic fatigue model fit was determined from the static fatigue results by applying the slow crack growth parameters in Table 3 to Equation 9c.

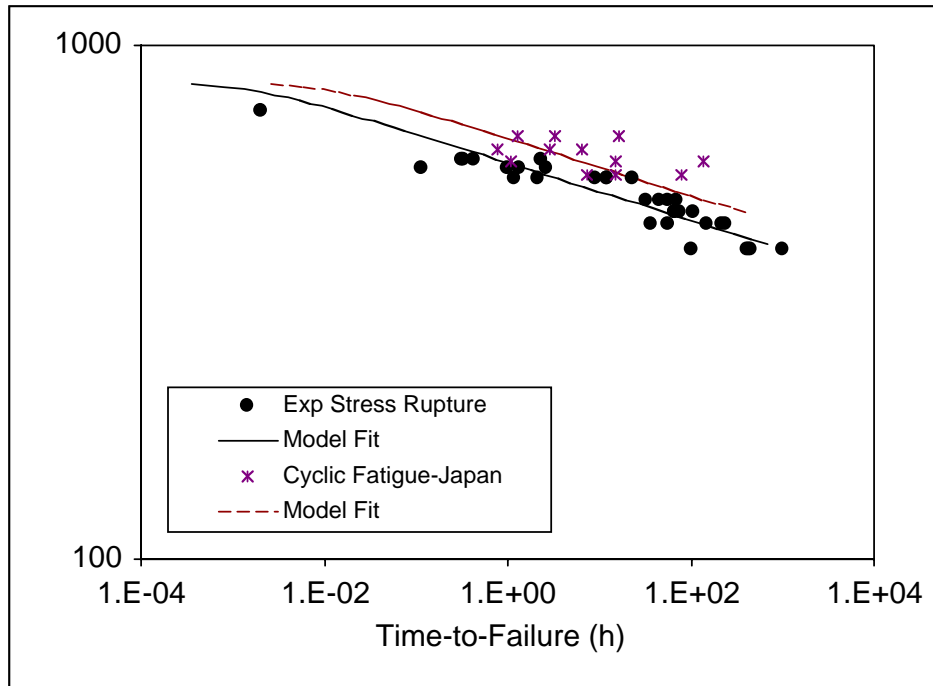


Figure 17: Comparison of static and cyclic fatigue results. The cyclic fatigue model fit was determined from the static fatigue results by applying the slow crack growth parameters in Table 3 to Equation 11.

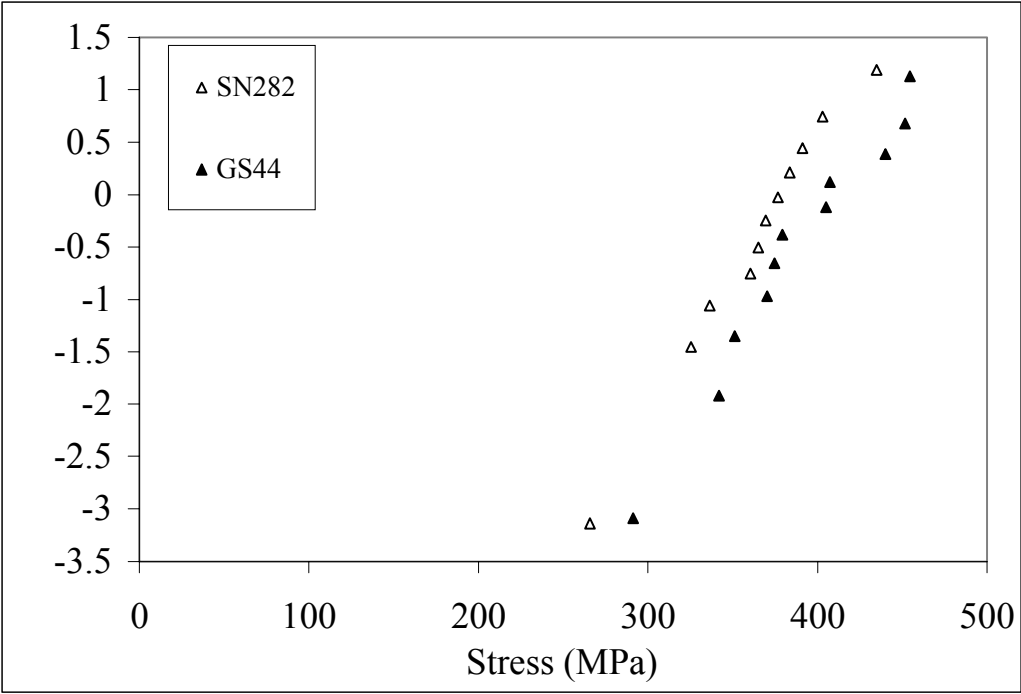


Figure 18: Weibull plots obtained from the thermal shock tests of the GS44 and SN282 silicon nitride ceramics.

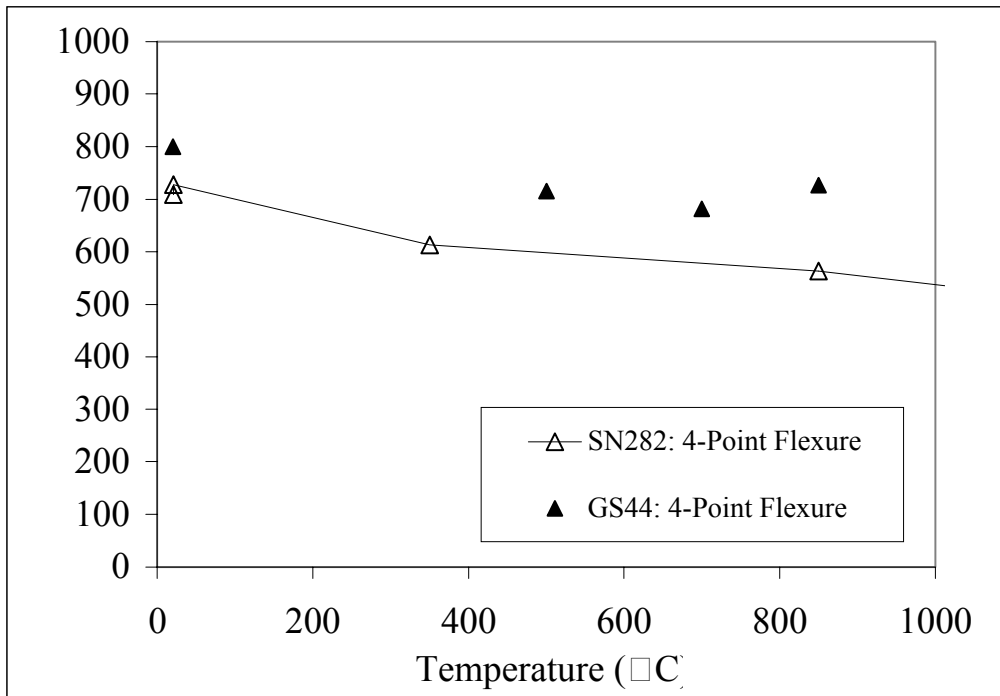


Figure 19: Weibull plots obtained from the thermal shock tests of the GS44 and SN282 silicon nitride ceramics.

expect that both materials exhibit higher thermal fracture strengths and that the average thermal fracture strength of the GS44 to be significantly higher than that of the SN282. This discrepancy may be a result of different flaw distributions present in the centrally-heated disk specimens.

As stated previously, the thermal fatigue experiments could be implemented due to problems in controlling the laser power as function of time.

## CONCLUSIONS

The GS44 silicon nitride was susceptible to slow crack growth at 850°C. This was reflected by the relative low value of the crack growth parameter,  $N (= 25)$ , estimated from the static fatigue of the flexure samples. The underlying mechanism was related to the softening of the intergranular phase, which resulted in extensive cavitation. The slow crack growth parameters determined by fitting the experimental static fatigue data to Equation 8b were found to adequately predict the dynamic fatigue and cyclic fatigue data obtained for the flexure bars.

Preliminary dynamic fatigue tests of the GS44 RBF specimens conducted at 850°C with no rotation exhibited no drop in strength with decreasing stressing rate. This result was attributed to excessive movement of the specimen, which was caused by creep of the grip collets at the slower loading rates. The application of a new dual acting loading geometry, which was intended to reduce the stresses on the grips, did not solve the problem. Future work must focus on the use of longer specimens such that grip heating is minimized.

The SN282 silicon nitride was not susceptible to fatigue at 850°C. However, previous testing conducted under the domestic task in Japan [6] showed that the SN282 was susceptible to strength degradation when subjected to cyclic loading at room temperature.

## REFERENCES

- [1] M. K. Ferber, Kirchoff, G., Hollstein, T., Westerheide, R. Bast, U., Rettig, U., and Mizuno, M., "Thermal Shock Testing of Advanced Ceramics – Subtask 9 (Final Report)," Oak Ridge National Laboratory, Oak Ridge, Tennessee, Report No. MOO-107208, March 2000.
- [2] A. A. Wereszczak, H.-T. Lin, T. P. Kirkland, "Strength and dynamic fatigue of silicon nitride at intermediate temperatures," *J. Mater. Sci.* **37** 2669 – 2684, (2002).
- [3] JIS R 1621, Test Method for Bending Fatigue of Fine Ceramics at Room Temperature (1995).
- [4] G. Kirchhoff, M. Holzherr, U. Bast, and U. Rettig, "Thermal Shock and Thermal Cycling Behavior of Silicon Nitride Ceramics," pp. 605-10 in Key Engineering Materials, Vol. 89-91, Trans Tech Publications (1994).

- [5] M. K. Ferber and M. G. Jenkins, "Evaluation of the Strength and Creep-Fatigue Behavior of a HIPed Silicon Nitride, " *J. Amer. Ceram. Soc.* , **75**, [9], 2453-62, 1992.
- [6] Mineo Mizuno and Yorinobu Takigawa , "Mechanical and Thermal Fatigue of Silicon Nitridewithin IEA Subtask 11-Japanese Final Report," Japan Fine Ceramics Center, January 2003.